Journal of Non-Crystalline Solids 525 (2019) 119671

Contents lists available at ScienceDirect

Journal of Non-Crystalline Solids

journal homepage: www.elsevier.com/locate/jnoncrysol

Effects of structural relaxation on the dye degradation ability of FePC amorphous alloys

Qianqian Wang[a], Mingxiu Chen[a], Liliang Shao[a], Youwen Ge[a], Pinghua Lin[a], Chenglin Chu[a,*], Baolong Shen[a,b,*]

[a] School of Materials Science and Engineering, Jiangsu Key Laboratory for Advanced Metallic Materials, Southeast University, Nanjing 211189, China
[b] Institute of Massive Amorphous Metal Science, China University of Mining and Technology, Xuzhou 221116, China

ARTICLE INFO

Keywords:
FePC amorphous alloys
Structural relaxation
Exothermic heat
Nanocrystals
Fenton-like reactions

ABSTRACT

The effects of structural relaxation on the catalytic efficiency of FePC amorphous ribbons in the Fenton-like reactions are studied. Different from previous knowledge, the catalytic efficiency of the Fe-based amorphous ribbons doesn't decrease linearly with increased annealing temperature before glass transition. The catalytic ability of the FePC ribbons annealed at 553 and 593 K is worse than that of as-quenched ribbons, while the ribbons treated isothermally at 633 and 673 K show higher catalytic efficiency. The impacts of structural relaxation on dye degradation performance should be considered from two aspects: i) The stored energy in the metastable ribbons, which comes from the high enthalpy and residue stress, decreases with increased annealing temperature, leading to the depression of degradation performance. ii) The precipitation of nanocrystals in the amorphous matrix when annealed at temperatures close to glass transition promotes the formation of galvanic cells that improve the catalytic efficiency of the ribbons.

1. Introduction

The extensive use of synthetic dyes in printing and dying industries, e.g. textile, leather and paint, has brought serious environmental problems, as most of the synthetic dyes can't be decomposed by the microorganisms in nature [1,2]. The residue synthetic dyes and their derivatives in the aquatic system are not only visually unpleasant, but also harmful to living beings as they are potentially carcinogenic and carcinogenic [3]. Tremendous efforts have been made to remove these contaminants from water resources. Compared with the biological treatments and physical adsorptions, the chemical methods, including zero-valent metals, bimetallic alloys, advanced oxidation processes (AOPs), etc., have more advantages due to their higher efficiency and lower cost [4–6]. Recently, amorphous alloys have been proved to be able to decompose synthetic dyes, COD, phenols, petroleum and other organic contaminants effectively and efficiently via the redox reactions and Fenton-like reactions [7–9]. Mg-, Co-, Al-, Cu-, and Fe-based amorphous alloys, in forms of powders, ribbons and nanoporous structures, have been reported for applications in dye degradation due to their thermodynamic metastable nature and a large amount of available reactive sites [10–18]. Among them, Fe-based amorphous alloys (FAAs) are chemically reactive and low-cost, and have the excellent soft-magnetic properties which can be applied in the auto-recycling process [19], thus attracted the most research attentions [20,21].

The effects of structural relaxation induced by annealing on the degradation ability of FAAs are controversial. Most researches showed that the dye degradation ability of FAAs decreased with increasing annealing temperatures [22–24]. However, Chen et al. and Wang et al. reported the improved azo dye decomposition efficiency by annealing the FAAs [$(Fe_{73.5}Si_{13.5}B_9Nb_3Cu_1)_{91.5}Ni_{8.5}$ and $Fe_{82.65}Si_4B_{12}Cu_{1.35}$] at high temperatures due to the formed galvanic cells between the precipitated multiple crystalline phases and residue amorphous matrix, respectively [25,26]. Jia et al. revealed that the compelling rejuvenated catalytic performance was achieved in the fully crystallized $Fe_{78}Si_9B_{13}$ and $Fe_{73.5}Si_{13.5}B_9Cu_1Nb_3$ ribbons after annealing treatment due to the formation of self-motived galvanic cells and reduced grain boundaries [27]. Our previous work showed that the $Fe_{81}Si_2B_{10}P_6Cu_1$ amorphous ribbons and their single-crystalline ribbons have higher catalytic efficiency than the multiple-crystalline ribbons, because the dye degradation ability of Fe-based amorphous/nanocrystalline alloys are controlled competitively by the positive impact from the galvanic cells formed between different phases and the negative influence from the oxidation layers formed during high-temperature annealing [28,29].

* Corresponding authors.
E-mail addresses: clchu@seu.edu.cn (C. Chu), blshen@seu.edu.cn (B. Shen).

https://doi.org/10.1016/j.jnoncrysol.2019.119671
Received 24 May 2019; Received in revised form 29 August 2019; Accepted 6 September 2019

Most of the studies about the relationship between structural relaxation and degradation ability of FAAs focused on high-temperature treatments and crystallization, the effect of structural relaxation before glass transition hasn't been well studied. Chen et al. carried out isothermal annealing on $(Fe_{73.5}Si_{13.5}B_9Nb_3Cu_1)_{91.5}Ni_{8.5}$ amorphous ribbons at 573 and 673 K, which are below the glass transition temperature (T_g) of 725 K [30]. They proposed that the dye decomposition efficiency of this alloy is reduced with increased annealing temperatures due to the decreasing of residue stress. However, the annealing treatment below T_g is a complex structural evolution process, not just a residue stress reduction behavior. And the temperature intervals they chose were too large to give enough information about the complicated impact from structural relaxation on the dye degradation efficiency.

Recently, $Fe_{80}P_{13}C_7$ amorphous ribbons were reported to have high potential for wastewater remediation as they have better catalytic efficiency than the most widely studied $Fe_{78}Si_9B_{13}$ amorphous ribbons, and show large reusability due to their "self-renewing" behavior [15]. Thus, in this work, the Fenton-like reactions were carried out using the $Fe_{80}P_{13}C_7$ ribbons annealed below T_g to study the effect of structural relaxation on the degradation ability of FAAs. Rhodamine B (RhB), which is a commonly used synthetic dye in shampoo, body wash, etc., and listed as cancerogen by World Health Organization (WHO), is adopted as the target to be degraded. It was found that the time required to finish degrade RhB increased with increasing annealing temperatures to 593 K first, and then decreased with further increasing the annealing temperatures up to 673 K (20 K below T_g). The stored energy in the metastable ribbons, including the high enthalpy and residue stress, reduces linearly with increasing annealing temperatures and explains the decrease of degradation efficiency. The appearance of nanocrystals in the ribbons after annealed at 633 and 673 K drives the formation of galvanic cell structures and improves the degradation efficiency. This work proves that the dye degradation efficiency of FAAs annealed below T_g is controlled by the reduction of stored energy in the metastable ribbons and the appearance of nanocrystals competitively, and gives a new approach to control the degradation efficiency of FAAs.

2. Experimental

2.1. Materials

Alloy ingots with a nominal composition of $Fe_{80}P_{13}C_7$ (at.%) were prepared by induction melting of high-purity Fe (99.99% wt%), pre-alloyed Fe—P ingots (75 at.% Fe and 25 at.% P) and Fe—C ingots (96 at.% Fe and 4 at.% C) in a purified argon atmosphere. Ribbons with a thickness of ~ 25 μm and a width of ~ 2 mm were prepared by single roller melt spinning method in a purified argon atmosphere. The as-quenched ribbons were then annealed at different temperatures. The isothermal annealing was carried out by keeping the ribbons in a pre-heated tubular furnace at annealing temperature for 5 min in a vacuum chamber followed by water quenching. The annealed ribbons were cut into 1 cm long for degradation experiments. Commercially available synthetic dye RhB ($C_{28}H_{31}ClN_2O_3$, AR grade) was purchased from Tianjin Chemical Reagent Research Institute. Sodium hydroxide (NaOH, AR grade) was purchased from Greagent. Sulphuric acid (H_2SO_4, AR grade) was purchased from Chron Chemicals. Hydro peroxide (H_2O_2, AR grade) was purchased from Sinopharm Chemical Reagent Co., Ltd.

2.2. Characterization

The amorphous structure of the as-quenched and annealed ribbons was verified by X-ray diffraction (XRD, Bruker D8 Discover) with Cu-Kα radiation. For nanostructure analyses, the ribbons were thinned carefully by a low-angle (5°) ion milling (GATAN-691) and then examined with a high resolution transmission electron microscope (TEM, FEI Tecnai G2 F20). The surface morphologies of the ribbons were analyzed using a scanning electron microscope (SEM, FEI Sirion 200). The thermal properties of the as-quenched ribbons were measured by a differential scanning calorimeter (DSC, NETZSCH 404 F3) at a heating rate of 40 K/min. To measure the heat of relaxation, the ribbons were heated from 303 K to 1073 K at 20 K/min, and then cooled down to 303 K quickly. A second run with the same experimental settings were carried out right after, and used as the baseline to be subtracted from the first cycle.

2.3. Chemical tests

The electrochemical properties were analyzed using an electrochemical measuring instrument (Gamry Interface 1000). The measurements were conducted in a three-electrode cell using a platinum counter electrode and an Ag/AgCl reference electrode. The potentiodynamic polarization curves were recorded at a potential sweep speed of 4 mV/s after the open circuit potentials were stabilized. The solutions used for both the polarization measurements and EIS tests were 50 mL acid RhB solution with H_2O_2 (T = 298 K, pH = 3, 1 mM H_2O_2, 50 mg/L RhB).

For dye decolorization tests, 250 mL RhB solution (50 mg/L) was prepared using deionized (DI) water in a 500 mL beaker. A specific amount of ribbons (0.5 g/L) and H_2O_2 (1 mM) were added to the solution, which was stirred at a fixed speed during the degradation process. The temperature of the solution was maintained at 298 K using a water bath. The initial pH (pH = 3) of the solution was adjusted using 5% H_2SO_4, as well as 1 M and 0.1 M NaOH. At the selected time intervals, 2.5 mL of the solution was extracted using a syringe and filtered with a 0.22 μm membrane, and then scanned using a UV–Vis spectrophotometer (Shimadzu UV-1280) to obtain the absorbance spectrum of the solution.

3. Results and discussion

The as-quenched FePC (AQ) ribbons are amorphous as only one diffuse halo appears on the XRD curve as shown in Fig. 1(b). DSC analysis of the AQ ribbons reveals that they have distinct glass transition phenomenon (T_g = 693 K) followed by a two-step crystallization, as shown in Fig. 1(a). Isothermal annealing was carried out on the AQ ribbons at 553, 593, 633 and 673 K, with the obtained annealed ribbons named as AN553, AN593, AN633 and AN673, respectively. All the annealed ribbons keep the amorphous structures as no sharp diffraction peak coming from crystalline phase is observed on the XRD curves shown in Fig. 1(b). This is because the annealing temperatures are below T_g and the annealing time is only 5 min.

In order to analyze the effects of structural relaxation on the catalytic ability of amorphous ribbons, the Fenton-like reactions for degrading RhB using AQ, AN553, AN593, AN633 and AN673 ribbons were carried out, and the reaction processes were monitored by UV–vis spectroscopy. The reaction parameters were set as: solution temperature T = 298 K, initial RhB concentration C_{RhB} = 50 mg/L, pH = 3, initial concentration of H_2O_2 $C_{H_2O_2}$ = 1 mM, ribbon dosage = 0.5 g/L. All the RhB solutions change to nearly transparent after degradation with the representative ones shown in Fig. 2(a), indicating the AQ and the annealed ribbons have catalytic capability. However, the time required for completing these decolorization processes are different. The UV–vis absorbance spectra of the RhB solutions at different reaction times using AQ, AN553, AN593, AN633 and AN673 ribbons are shown in Fig. 2(b–f), respectively. The intensity of the peaks decreases with reaction time, revealing the reduction of RhB concentration. The major absorbance peak for RhB is at 554 nm, which is used to quantitatively calculate the concentration of RhB solutions [31]. Apparently, RhB is completely degraded when the peak at 554 nm (P_{554}) disappears. The normalized concentration of RhB at different reaction time for the five kinds of ribbons are calculated based on the changes of UV–vis adsorption intensity at P_{554}, and plotted in Fig. 3(a). C_t represents the

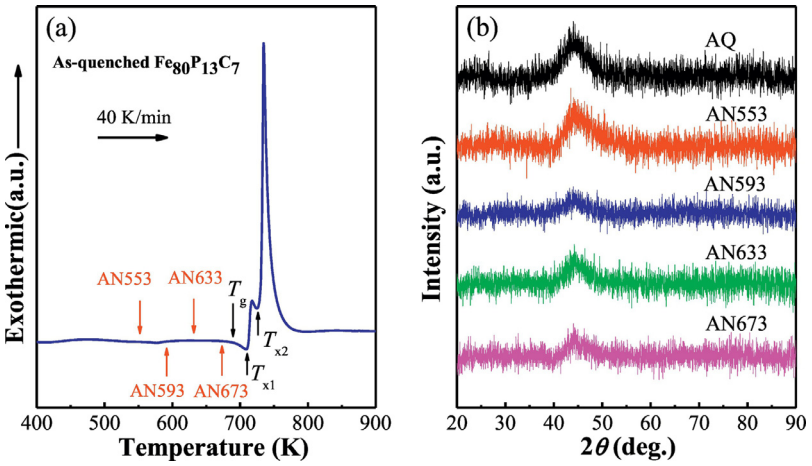

Fig. 1. (a) DSC analysis of the as-quenched FePC amorphous ribbon. The glass transition temperature (T_g), and onset temperatures of the two crystallization peaks (T_{x1} and T_{x2}) are pointed out by the black arrows. The annealing temperatures of the ribbons are pointed out by the red arrows. (b) XRD analyses of the AQ, AN553, AN593, AN633 and AN673 ribbons. (For interpretation of the references to colour in this figure legend, the reader is referred to the web version of this article.)

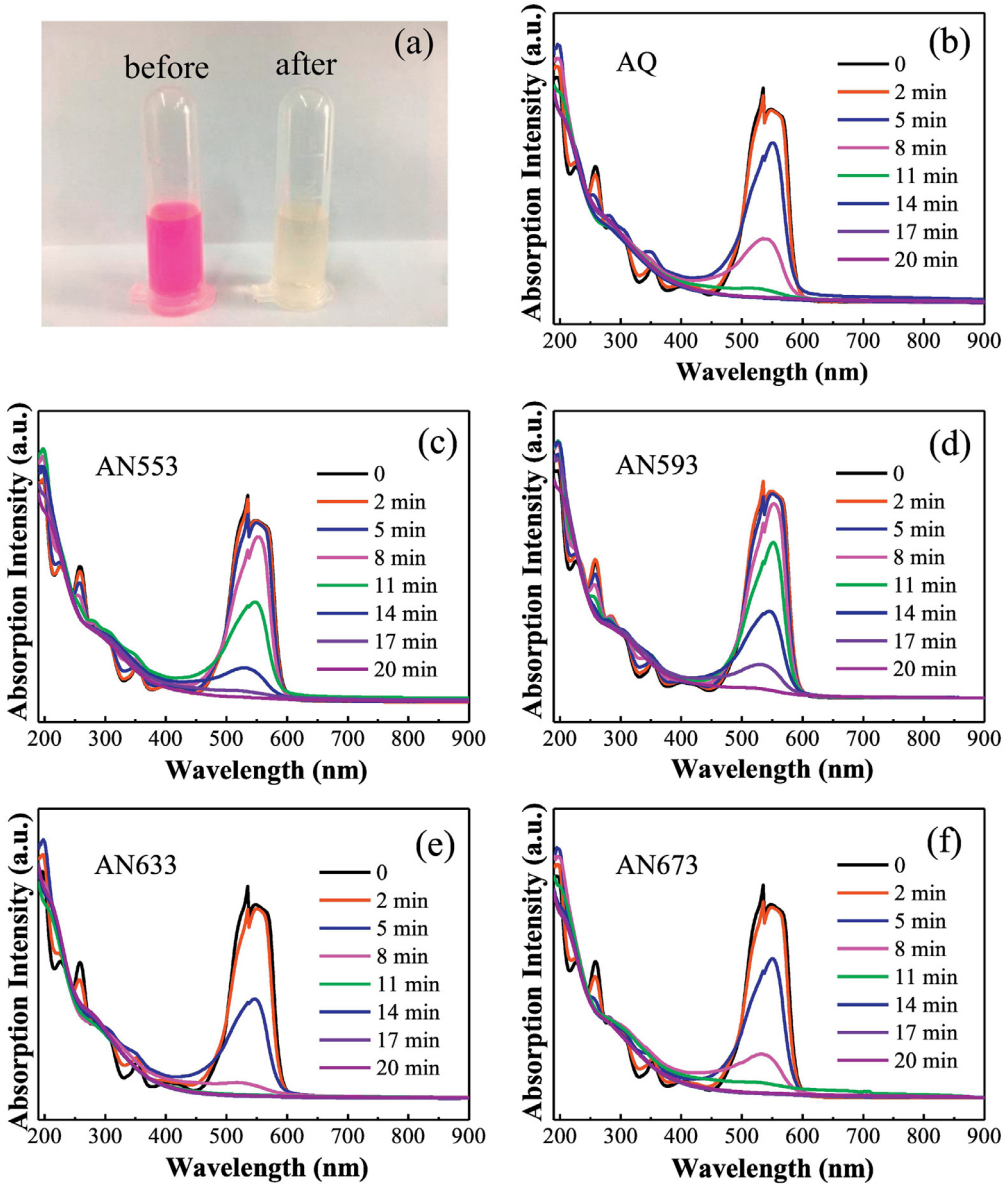

Fig. 2. (a) The optical image of the RhB solutions before and after degradation. (b–f) UV-vis absorbance plots of the RhB solutions at different time intervals during the Fenton-like reactions using AQ, AN553, AN593, AN633 and AN673 ribbons, respectively.

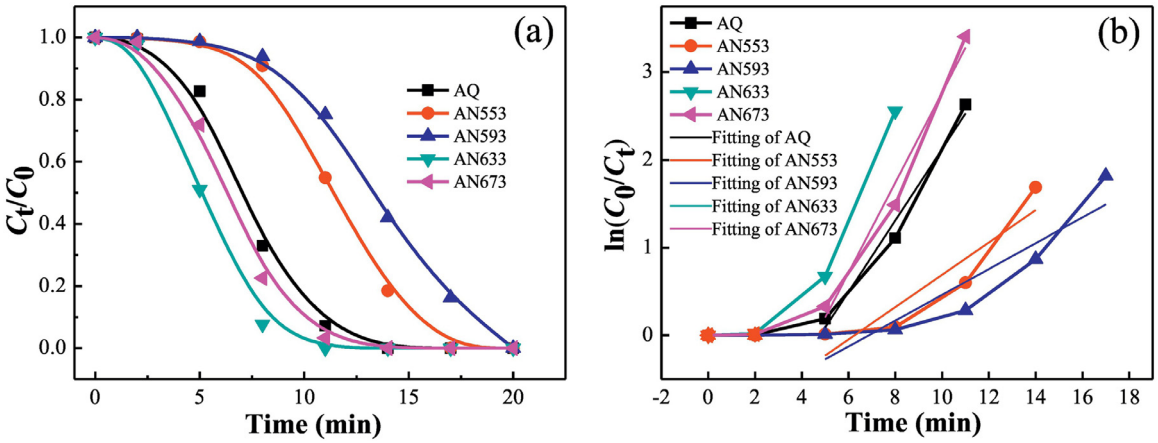

Fig. 3. (a) The normalized concentration change of RhB solutions during the Fenton-like reactions using AQ, AN553, AN593, AN633 and AN673 ribbons. (b) The ln (C_0/C_t) vs. time curves for the Fenton-reactions using AQ, AN553, AN593, AN633 and AN673 ribbons.

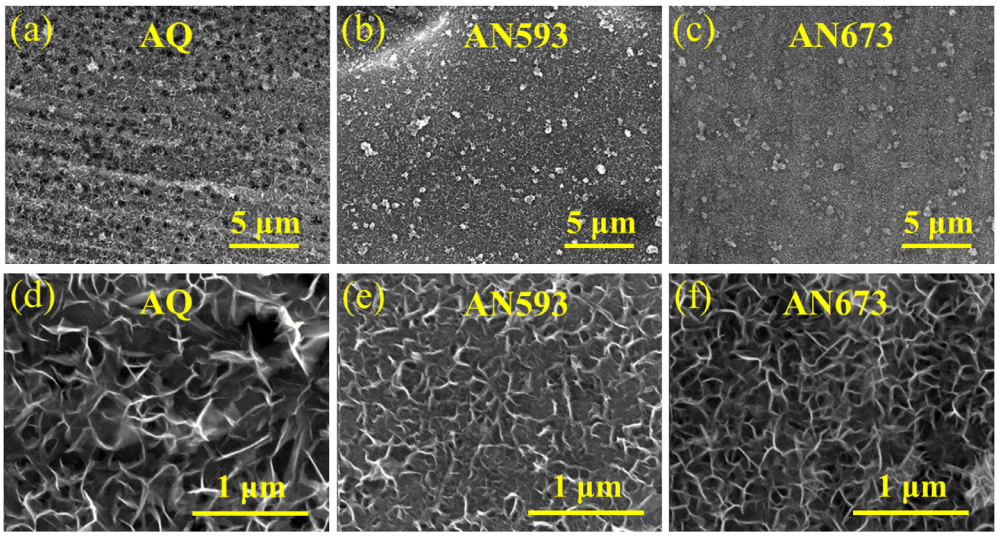

Fig. 4. The SEM images of reacted (a, d) AQ ribbons, (b, e) AN593 and (c, f) AN673 ribbons.

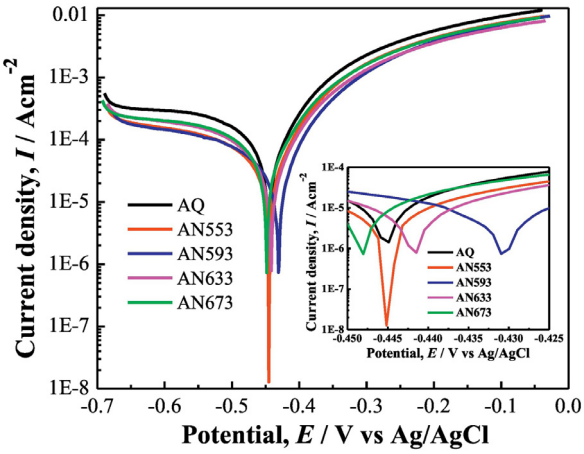

Fig. 5. The potentiodynamic polarization curves of the AQ, AN553, AN593, AN633 and AN673 ribbons in the RhB solutions (T = 298 K, C_{RhB} = 50 mg/L, pH = 3, C_{H2O2} = 1 mM). The inset shows the enlarged polarization curves.

instant intensity of P_{554} at reaction time t (min), while C_0 represents the intensity of P_{554} before reaction. In this work, the RhB degradation process is considered to be completed when C_t/C_0 is less than 5% due to the instrumental fluctuation. Based on the C_t/C_0 vs. time curves, the AQ ribbons are able to finish degrading RhB within 14 min. The reaction time for AN553 and AN593 ribbons increases to 17 and 20 min, respectively. Surprisingly, by further increasing the annealing temperatures to 633 and 673 K, the catalytic efficiency of the ribbons is improved. Both of the AN633 and AN673 ribbons need only 11 min to complete the degradation processes, which are even better than the as-quenched ones. The degradation kinetics are commonly described by the pseudo-first-order equation as shown below [32]:

$$C_t = C_0 * \exp(-kt) \quad (1)$$

where k is the reaction rate constant (min^{-1}). Thus, the k values of each reaction can be derived by the following equation:

$$k = \mathrm{In}\left(\frac{C_0}{C_t}\right)/t \quad (2)$$

The $\ln(C_0/C_t)$ vs. t curves are plotted in Fig. 3(b), and k values are equal to the slopes of the linear fittings of the curves. The reaction rate constants for AQ, AN553, AN593, AN633 and AN673 are 0.41, 0.18, 0.15, 0.63 and 0.51 min^{-1}, respectively. The variations of k values are consistent with the normalized concentration change curves, confirming the reactions using the ribbons annealed at 633 and 673 K are accelerated compared with the one using AQ ribbons.

The degradation ability of the ribbons is largely affected by the change of surface morphology during the reaction process [17]. SEM

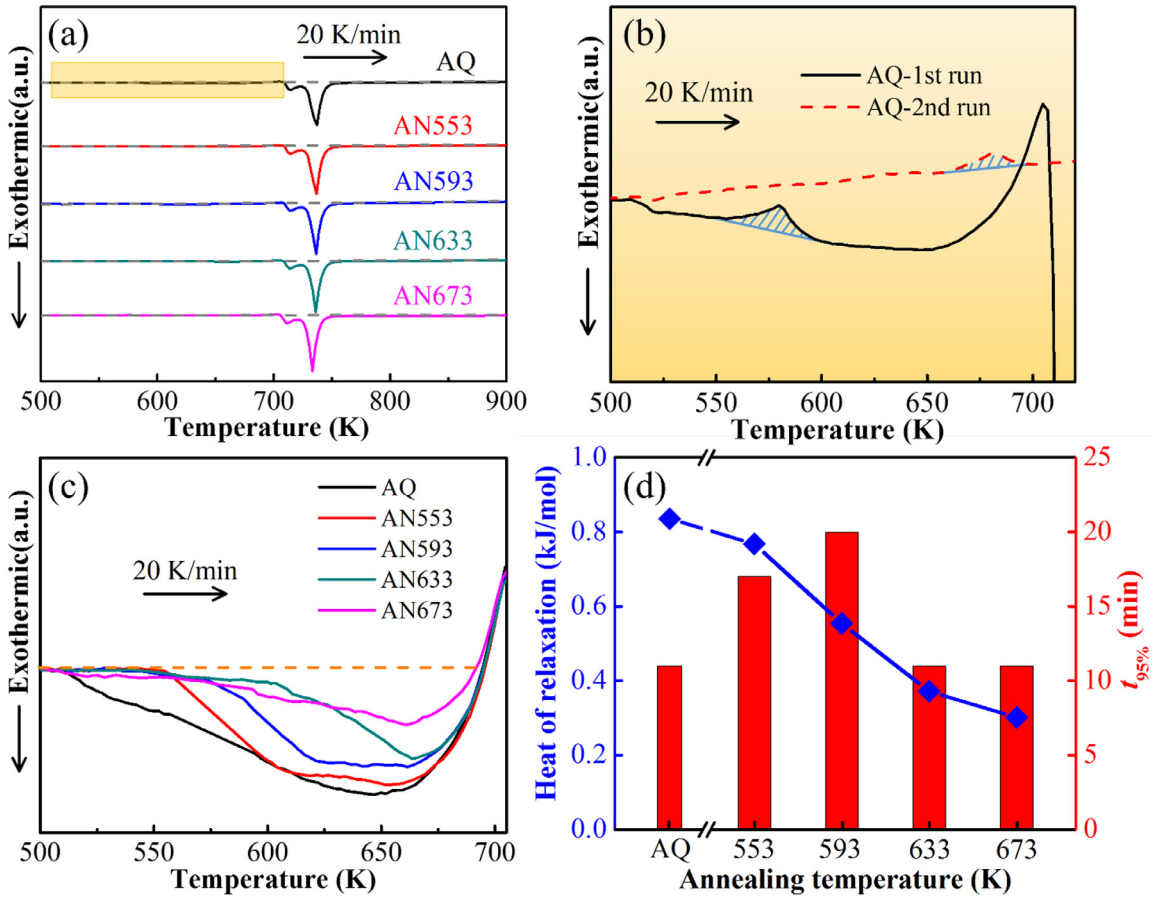

Fig. 6. (a) The DSC curves of the AQ, AN553, AN593, AN633 and AN673 ribbons for the heat of relaxation measurements. The DSC curves from the second run that were used as the baselines to be subtracted are shown by the grey dashed lines. (b) DSC curves of the AQ ribbons from the two heating processes. The shaded areas indicate the endothermal peaks for T_c. (c) The DSC curves of the ribbons with baselines subtracted focusing on the temperature range showing the exothermic heat before T_g. (d) Comparison of the exothermic heat and the time required for degrading 95% of RhB.

images of the surface of AQ, AN593 and AN673 ribbons after degradation are shown in Fig. 4(a–c), and their enlarged images are shown in Fig. 4(d–f), respectively. All of the three kinds of reacted ribbons show 3D nanoporous structures on the surface, indicating the excellent catalytic ability of FePC amorphous alloys. However, the size of the pores on the surface of AQ and AN673 ribbons seems to be larger than that of AN593 ribbon. Besides, there is a thin film covering the nanoporous structures on the surface of AN593 ribbon. Both the smaller pore size and the covering film impede mass and electron transportation for the Fenton-like reaction using AN593 ribbons, and lower its catalytic efficiency.

As the Fenton-like reaction involves the electron donation of zero-valent iron from the alloy, the corrosion resistance, which is inversely related to the electron donation ability, is an important parameter to evaluate the catalytic efficiency of FAAs. The electrochemical properties of the ribbons were measured by the potentiodynamic polarization tests carried on the ribbons in RhB solutions (T = 298 K, C_{RhB} = 50 mg/L, pH = 3, $C_{H_2O_2}$ = 1 mM), with the curves shown in Fig. 5. All the polarization curves of the five kinds of ribbons show an anodic polarization without passive regions, indicating no compact passive oxidation layer forms on the ribbon surface during the reactions. This is consistent with the SEM analyses in Fig. 4, and further prove the high catalytic efficiency of FePC amorphous alloys. Although the corrosion potentials of the five kinds of ribbons are within a small range (−0.425∼ −0.450 V), the electrochemical parameters can still be distinguished in the enlarged polarization curves shown in the inset of Fig. 5. Compared with the AQ ribbon, the AN553 ribbon has a similar corrosion potential but a much lower corrosion current density, revealing the corrosion resistance is slightly improved by annealing the AQ ribbons at 553 K. The corrosion potential of AN593 ribbon is the highest among all the ribbons, indicating its best corrosion resistance in the solution. By further increasing the annealing temperatures to 633 and 673 K, the corrosion resistance of the ribbons is reduced as the corrosion potentials of the ribbons keep decreasing linearly. The corrosion potential of AN673 ribbon is even lower than the AQ ribbon. The first improved then decreased corrosion resistance of the ribbons with increased annealing temperatures are consistent with their degradation performance revealed in Figs. 2 and 3.

The thermodynamically unstable nature and the large residue stress of amorphous alloys, both of which come from the large cooling rate during casting, are believed to be the main reasons for the high catalytic efficiency of FAAs. Isothermal annealing is a process for the metastable structures to relax, which means the enthalpy and residue stress of the FAAs should reduce after annealing [30,33]. DSC analysis has been proved to be an effective method to compare the structural relaxation degree of FAAs [34]. During heating process, the exothermic heat (ΔH_{rel}) before T_g measured by DSC represents the released energy before glass transition. In this work, the as-quenched and annealed ribbons were analyzed by DSC at a heating rate of 20 K/min, which is much lower than the cooling rate that FAAs were formed. A second DSC run was carried out right after each heating process and subtracted as the baseline, indicated by the grey dashed lines shown in Fig. 6(a). The DSC curves of the annealed ribbons are similar to the AQ ribbon, which go through a two-step crystallization process during heating. Before comparing the heat of relaxation of the ribbon, several issues have to be mentioned here. Ferromagnetic alloys, especially Fe-based alloys, go

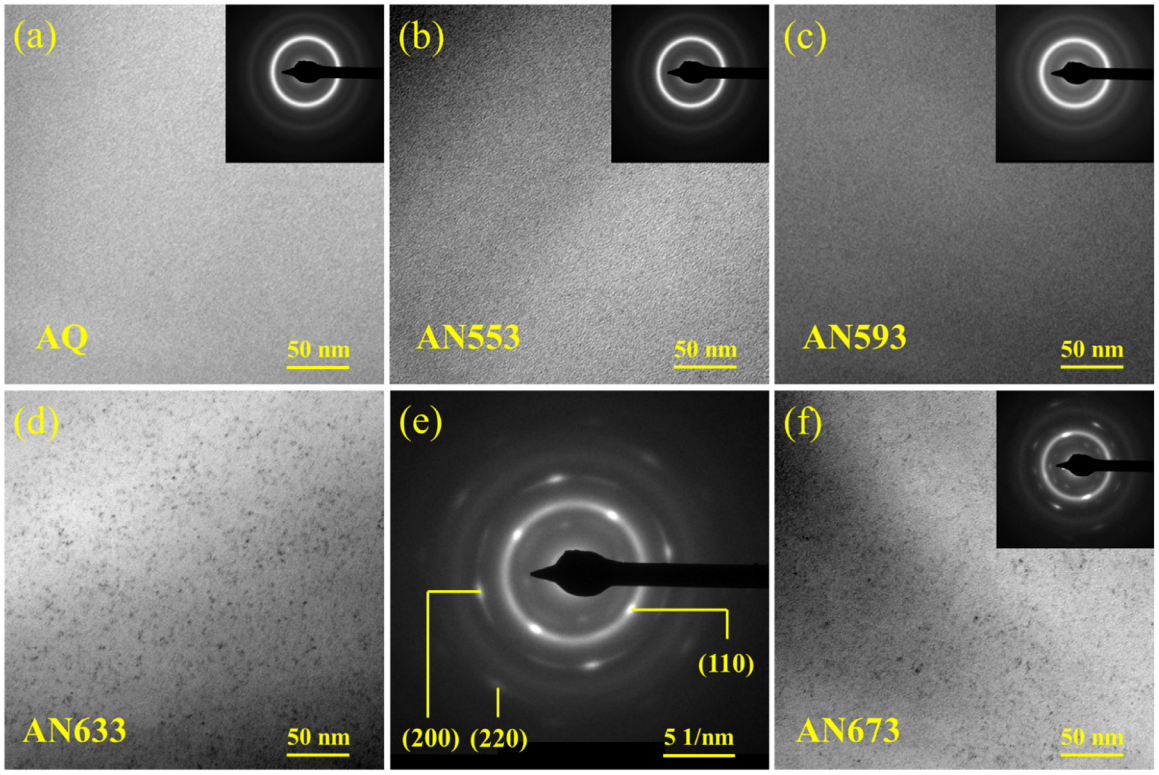

Fig. 7. (a–c, f) The TEM images of AQ, AN553, AN593 and AN673 ribbons, with insets showing the corresponding SAED patterns. (d) The TEM and (e) corresponding SAED pattern of AN633 ribbon.

through the ferromagnetic to paramagnetic transitions during heating. The temperature for this transition is defined as Curie temperature (T_c). The magnetic transition at T_c is a second-order phase transition and can be captured as an endothermic peak on the heating DSC curves. To give an example, the two heating DSC curves of AQ ribbons focusing on the specific heat regions before T_g [as indicated by the yellow square in Fig. 6(a)] are shown in Fig. 6(b). After the first heating process, the ribbon was completely crystalized, thus its T_c at the second heating run (the one used as a baseline to be subtracted from the first heating DSC curve) increases about 100 K. For crystalized ribbons, the movements of the magnetic domains are largely impeded by the formed abundant grain boundaries, and a higher input energy is required to induce the ferromagnetic to paramagnetic transition. As a result, the T_c peak at the second run moves to a higher temperature [35]. As the endothermic heat caused by the ferromagnetic to paramagnetic transition is a magnetic behavior, it should not be included in the heat of relaxation calculations for the ribbons. The areas under the T_c peaks are subtracted before further analysis. For all the ribbons, the areas under the T_c peaks of the first run are usually about 0.09 kJ/mol larger than those of the second run. By eliminating the influence from T_c, the exothermic curves before T_g can be compared for the ribbons, as shown in Fig. 6(c). The areas between the DSC curves and the baseline (dashed orange line) are taken as the exothermic heat, with the value of each sample summarized in Fig. 6(b). As expected, the ΔH_{rel} of the annealed ribbons are smaller than the AQ ribbon due to the structural relaxation. Besides, the ΔH_{rel} decreases with the increasing annealing temperature linearly as a larger degree of structural relaxation can be expected at higher temperature. Thus, if the high-energy state and the large residue stress of FAAs are the only contributions for the high catalytic efficiency, the time required for the RhB degradation should increases linearly with the increasing annealing temperature. However, only the ribbons annealed at lower temperatures (AN553 and AN593) need more time to finish the degradation process, while the ribbons annealed at higher temperatures (AN633 and AN673) show higher efficiency than the AQ ribbons. To unveil the reason for this confliction, nanostructures of the ribbons were analyzed using TEM.

The TEM micrographs and corresponding selected area diffraction (SAED) patterns of the as-quenched and annealed ribbons are shown in Fig. 7. No crystallite is observed on the TEM images of the AQ, AN533 and AN593 ribbons, and their corresponding SAED patterns only consist of broad diffuse halos. These features confirm the complete amorphous structures in the AQ, AN533 and AN593 ribbons. When the annealing temperatures increase to 633 and 673 K, small nanocrystals precipitate all over the amorphous matrix, as shown in Fig. 7(d, f). The SAED pattern of the corresponding TEM image of AN633 is shown in Fig. 7(e). By analyzing the lattice distances of the three major diffraction rings, the precipitates are confirmed to be α-Fe phase. The SAED pattern of AN673 [inset of Fig. 7(f)] also shows the existence of α-Fe phase. The precipitation of α-Fe as the initial crystallization phase in FePC amorphous alloy has been revealed by in situ neutron diffraction studies [36]. These α-Fe nanocrystals are generally less than 1.5 nm, which are too tiny to be detected by the XRD analyses. As the GFA of the ternary FePC amorphous alloy is small, and the annealing temperatures of AN633 and AN 673 ribbons are only 60 and 20 K below T_g, respectively, the precipitation of the nanocrystals is not difficult to be understood. It is well accepted that galvanic cells can form between different phases in the high-temperature annealed amorphous alloys due to the electrochemical potential differences between the crystalline phases and amorphous matrix. The galvanic cells structures can improve the electron donation rate of zero-valent iron effectively, which results in the enhancement of the catalytic efficiency of FAAs. Thus, the structural heterogeneity from the precipitated nanocrystals in the AN633 and AN673 ribbons, which induces the formation of galvanic cells [28], plays a positive role during RhB degradation, and overcomes the negative impacts from the reduced thermodynamic enthalpy and residue stress. As a result, the competition between the structural heterogeneity and the reduced energy/residue stress in AN633 and AN673 leads to their recovery of catalytic efficiency.

4. Conclusions

The effects of structural relaxation on the catalytic efficiency of FePC amorphous ribbons in the Fenton-like reactions were studied in detail. By increasing the annealing temperature, the catalytic ability of the ribbons was reduced when annealed at 553 and 593 K, and then improved (even better than the AQ ribbons) after treated isothermally at 633 and 673 K. The impacts of structural relaxation on the RhB degradation performance for the ribbons should be considered from two aspects: i) The enthalpy and the residue stress in the ribbons decrease with increasing annealing temperature, leading to the depression of degradation performance. ii) The precipitation of small nanocrystals in the amorphous matrix when annealed at temperatures close to T_g promotes the formation of galvanic cells that can effectively improve the catalytic efficiency of the ribbons. The competition between the two impacts leads to the overall performance of annealed ribbons. This work provides insights of improving the catalytic efficiency by tuning the structural relaxation of FAAs.

Declaration of Competing Interest

The authors declared that they have no conflicts of interest to this work. We declare that we do not have any commercial or associative interest that represents a conflict of interest in connection with the work submitted.

Acknowledgements

This work was supported by the National Natural Science Foundation of China (Grant Nos. 51631003 and 51771054), and the Fundamental Research Funds for the Central Universities (Grant No. 2242019k1G005).

References

[1] I.K. Konstantinou, T.A. Albanis, TiO_2-assisted photocatalytic degradation of azo dyes in aqueous solution: kinetic and mechanistic investigations – a review, Appl. Catal. B-Environ. 49 (2004) 1–14.
[2] T.A. Saleh, Advanced Nanomaterials for Water Engineering, Treatment, and Hydraulics, IGI Global, Hershey, PA, USA, 2017, pp. 1–384.
[3] T. Robinson, G. McMullan, R. Marchant, P. Nigam, Remediation of dyes in textile effluent: a critical review on current treatment technologies with a proposed alternative, Bioresour. Technol. 77 (2001) 247–255.
[4] E.G. Garrido-Ramirez, B.K.G. Theng, M.L. Mora, Clays and oxide minerals as catalysts and nanocatalysts in Fenton-like reactions – a review, Appl. Clay Sci. 47 (2010) 182–192.
[5] A.D. Bokare, R.C. Chikate, C.V. Rode, K.M. Paknikar, Effect of surface chemistry of Fe-Ni nanoparticles on mechanistic pathways of azo dye degradation, Environ. Sci. Technol. 41 (2007) 7437–7443.
[6] P.D. Mines, J. Byun, Y. Hwang, H.A. Patel, H.R. Andersen, C.T. Yavuz, Nanoporous networks as effective stabilisation matrices for nanoscale zero-valent iron and groundwater pollutant removal, J. Mater. Chem. A 4 (2016) 632–639.
[7] X.C. Xu, K.Q. Qiu, Y.L. Ren, Z.L. Shi, Application of Fe78Si9B13 amorphous ribbon on the treatment of simulated petroleum wastewater by Fenton-like process, Mater Res. Express 6 (2019).
[8] J.F. Yang, X.F. Bian, Y.W. Bai, X.Q. Lv, P. Wang, Rapid organism degradation function of Fe-based alloys in high concentration wastewater, J. Non-Cryst. Solids 358 (2012) 2571–2574.
[9] Z. Deng, C. Zhang, L. Liu, Chemically dealloyed MgCuGd metallic glass with enhanced catalytic activity in degradation of phenol, Intermetallics 52 (2014) 9–14.
[10] C. Yang, C. Zhang, L. Liu, Excellent degradation performance of 3D hierarchical nanoporous structures of copper towards organic pollutants, J. Mater. Chem. A 6 (2018) 20992–21002.
[11] J.Q. Wang, Y.H. Liu, M.W. Chen, D.V. Louzguine-Luzgin, A. Inoue, J.H. Perepezko, Excellent capability in degrading azo dyes by MgZn-based metallic glass powders, Sci. Rep.-UK 2 (2012).
[12] X.D. Qin, Z.W. Zhu, G. Liu, H.M. Fu, H.W. Zhang, A.M. Wang, H. Li, H.F. Zhang, Ultrafast degradation of azo dyes catalyzed by cobalt-based metallic glass, Sci. Rep.-UK 5 (2015) 18226.
[13] C.Q. Zhang, Q.L. Sun, K.G. Liu, From adsorption to reductive degradation: different decolorization properties of metallic glasses based on different iron-group elements, J. Alloys Compd. 741 (2018) 1040–1047.
[14] P.P. Wang, J.Q. Wang, H. Li, H. Yang, J.T. Huo, J.G. Wang, C.T. Chang, X.M. Wang, R.W. Li, G. Wang, Fast decolorization of azo dyes in both alkaline and acidic solutions by Al-based metallic glasses, J. Alloys Compd. 701 (2017) 759–767.
[15] Q.Q. Wang, M.X. Chen, P.H. Lin, Z.Q. Cui, C.L. Chu, B.L. Shen, Investigation of FePC amorphous alloys with self-renewing behaviour for highly efficient decolorization of methylene blue, J. Mater. Chem. A 6 (2018) 10686.
[16] Z. Deng, X.H. Zhang, K.C. Chan, L. Liu, T. Li, Fe-based metallic glass catalyst with nanoporous surface for azo dye degradation, Chemosphere 174 (2017) 76–81.
[17] Z. Jia, Q. Wang, L.G. Sun, Q. Wang, L.C. Zhang, G. Wu, J.H. Luan, Z.B. Jiao, A.D. Wang, S.X. Liang, M. Gu, J. Lu, Attractive in situ self-reconstructed hierarchical gradient structure of metallic glass for high efficiency and remarkable stability in catalytic performance, Adv. Funct. Mater. 29 (2019) 1807857.
[18] L. Hou, Q.Q. Wang, X.D. Fan, F. Miao, W.M. Yang, B.L. Shen, Effect of Co addition on catalytic activity of FePCCu amorphous alloy for methylene blue degradation, New J. Chem. 43 (2019) 6126–6135.
[19] W.M. Yang, Q.Q. Wang, W.Y. Li, L. Xue, H.S. Liu, J. Zhou, J.Y. Mo, B.L. Shen, A novel thermal-tuning Fe-based amorphous alloy for automatically recycled methylene blue degradation, Mater Des. 161 (2019) 136–146.
[20] L.C. Zhang, S.X. Liang, Fe-based metallic glasses in functional catalytic applications, Chem.-Asian J. 13 (2018) 3575–3592.
[21] L.C. Zhang, Z. Jia, F.C. Lyu, S.X. Liang, J. Lu, A review of catalytic performance of metallic glasses in wastewater treatment: recent progress and prospects, Prog. Mater. Sci. 105 (2019).
[22] S.H. Xie, P. Huang, J.J. Kruzic, X.R. Zeng, H.X. Qian, A highly efficient degradation mechanism of methyl orange using Fe-based metallic glass powders, Sci. Rep.-UK 6 (2016) 21947.
[23] Z. Jia, J.C. Wang, S.X. Liang, W.C. Zhang, W.M. Wang, L.C. Zhang, Activation of peroxymonosulfate by Fe78Si9B13 metallic glass: the influence of crystallization, J. Alloys Compd. 728 (2017) 525–533.
[24] C.Q. Fu, L.J. Xu, Z.H. Dan, F.X. Qin, A. Makino, H. Chang, N. Hara, Annealing effect of amorphous Fe-Si-B-P-Cu precursors on microstructural evolution and redox behavior of nanoporous counterparts, J. Alloys Compd. 726 (2017) 810–819.
[25] S.Q. Chen, G.N. Yang, S.T. Luo, S.J. Yin, J.L. Jia, Z. Li, S.G. Gao, Y. Shao, K.F. Yao, Unexpected high performance of Fe-based nanocrystallized ribbons for azo dye decomposition, J. Mater. Chem. A 5 (2017) 14230–14240.
[26] P.P. Wang, J.Q. Wang, J.T. Huo, W. Xu, X.M. Wang, G. Wang, Fast degradation of azo dye by nanocrystallized Fe-based alloys, Sci. China Phys. Mech. 60 (2017).
[27] S.X. Liang, Z. Jia, Y.J. Liu, W.C. Zhang, W.M. Wang, J. Lu, L.C. Zhang, Compelling rejuvenated catalytic performance in metallic glasses, Adv. Mater. 30 (2018).
[28] Q.Q. Wang, L. Yun, M.X. Chen, D.D. Xu, Z.Q. Cui, Q.S. Zeng, P.H. Lin, C.L. Chu, B.L. Shen, Competitive effects of structural heterogeneity and surface chemical states on catalytic efficiency of FeSiBPCu amorphous and nanocrystalline alloys, Acs Appl. Nano Mater. 2 (2019) 214–227.
[29] H.X. Li, Z.C. Lu, S.L. Wang, Y. Wu, Z.P. Lu, Fe-based bulk metallic glasses: glass formation, fabrication, properties and applications, Prog. Mater. Sci. 103 (2019) 235–318.
[30] S.Q. Chen, Y. Shao, M.T. Cheng, K.F. Yao, Effect of residual stress on azo dye degradation capability of Fe-based metallic glass, J. Non-Cryst. Solids 473 (2017) 74–78.
[31] X.F. Wang, Y. Pan, Z.R. Zhu, J.L. Wu, Efficient degradation of rhodamine B using Fe-based metallic glass catalyst by Fenton-like process, Chemosphere 117 (2014) 638–643.
[32] Z. Jia, W.C. Zhang, W.M. Wang, D. Habibi, L.C. Zhang, Amorphous Fe78Si9B13 alloy: an efficient and reusable photo-enhanced Fenton-like catalyst in degradation of cibacron brilliant red 3B-A dye under UV-vis light, Appl. Catal. B-Environ. 192 (2016) 46–56.
[33] P. Murali, U. Ramamurty, Embrittlement of a bulk metallic glass due to sub-T-g annealing, Acta Mater. 53 (2005) 1467–1478.
[34] S.V. Ketov, Y.H. Sun, S. Nachum, Z. Lu, A. Checchi, A.R. Beraldin, H.Y. Bai, W.H. Wang, D.V. Louzguine-Luzgin, M.A. Carpenter, A.L. Greer, Rejuvenation of metallic glasses by non-affine thermal strain, Nature 524 (2015) 200.
[35] M.E. McHenry, M.A. Willard, D.E. Laughlin, Amorphous and nanocrystalline materials for applications as soft magnets, Prog. Mater. Sci. 44 (1999) 291–433.
[36] C. Tete, M. Vergnat, G. Marchal, P. Mangin, Some aspects of the precipitation of Fe-alpha crystallites in the FePC amorphous alloy, Solid State Commun. 53 (1985) 191–195.